Bubble casting soft robotics

Trevor Jones, Etienne Jambon-Puillet, Joel Marthelot, P.-T. Brun

Bubble Casting Soft Robotics

Trevor J. Jones,[1] Etienne Jambon-Puillet,[1] Joel Marthelot,[1,2] P.-T. Brun,[1*]
[1]Department of Chemical and Biological Engineering,
Princeton University, Princeton, NJ 08540, USA
[2]Aix-Marseille University, CNRS,
IUSTI, 13013, Marseille, France

Inspired by living organisms, soft robots are developed from intrinsically compliant materials enabling continuous motions mimicking animal and vegetal movement [1]. In soft robots, the canonical hinges and bolts are replaced by elastomers assembled into actuators programmed to change shape following the application of stimuli, e.g. pneumatic inflation [2–5]. The morphing information is typically directly embedded within the shape of these actuators, whose assembly is facilitated by recent advances in rapid prototyping techniques [6–11]. Yet, these manufacturing processes have limitations in scalability, design flexibility and robustness. Here we demonstrate a new all-in-one methodology for the fabrication and the programming of soft machines. Instead of relying on the assembly of individual parts, our approach harnesses interfacial flows in elastomers that progressively cure to robustly produce monolithic pneumatic actuators whose shape can easily be tailored to suit applications ranging from artificial muscles to grippers. We rationalize the fluid mechanics at play in the assembly of our actuators and model their subsequent morphing. We leverage this quantitative knowledge to program these soft machines and produce complex functionalities, e.g. sequential motion obtained from a monotonic stimulus. We expect that the flexibility, robustness and predictive nature of our methodology will accelerate the proliferation of soft robotics by enabling the assembly of complex actuators, e.g. long, tortuous or vascular structures, thereby paving the way towards new functionalities stemming from geometric and material nonlinearities.

Soft robots can achieve complex tasks such as gentle gripping, crawling, or swimming [3, 12, 13] using low-complexity, muscle-like soft actuators that bend, twist, contract, or elongate on demand [2, 5, 14–16]. This unique combination of softness and bioinspired motion make soft robots appealing for a variety of innovative applications where rigid robots would fail [17]. This blooming field is fueled by recent insights in modeling, computations and manufacturing that enable the design, the programming and the assembly of various kinds of soft machines. While chemically, thermally, electrically or magnetically activated soft actuators have been demonstrated [18–24], silicone bodied pneumatic robots powered by pressurized voids have drawn considerable attention owing to their simple and rapid actuation [25, 26]. The kinematics of such robots is encoded in the actuator flesh, i.e. shape or material, such that a change of internal pressure is mechanically converted into specific motion [27]. Manufacturing soft pneumatic actuators, particularly the void, is non-trivial and is usually accomplished with sequential molding procedures and removable frameworks that are tailored for specific actuators. Likewise, state-of-the-art film coating techniques [9–11] are restricted to simple geometries, while freeform fabrication techniques [7, 8] typically lack scalability and require long printing times. Often, the inflation of these actuators is hard to predict such that trial and error or long simulations are required to tailor the shape of the actuator for specific applications. Additionaly, soft pneumatic robots assembled from these actuators need to perform complex or sequential motion which typically require several actuators with independent fluid sources [28].

Here we introduce *bubble casting*, a simple and versatile fabrication methodology to assemble monolithic actuators programmed using the rules and tools of fluid mechanics. Fig. 1a and Movie S1 illustrate our approach involving elastomers that spontaneously cure when reagents are mixed (see Methods). We first fill a tubular mold by injecting uncured elastomer melt. While the melt is still liquid, we inject air to form an elongated bubble that creates the inner void of the actuator (Fig. 1ai). Gravity then sculpts the actuator by draining the polymer film and allowing the bubble to rise (Fig. 1aii). Eventually, as the melt solidifies this shape is *frozen* and the actuator can be readily used when de-molded, e.g. as a gripper (Fig. 1aiii). In the following we demonstrate how to control bubble casting to

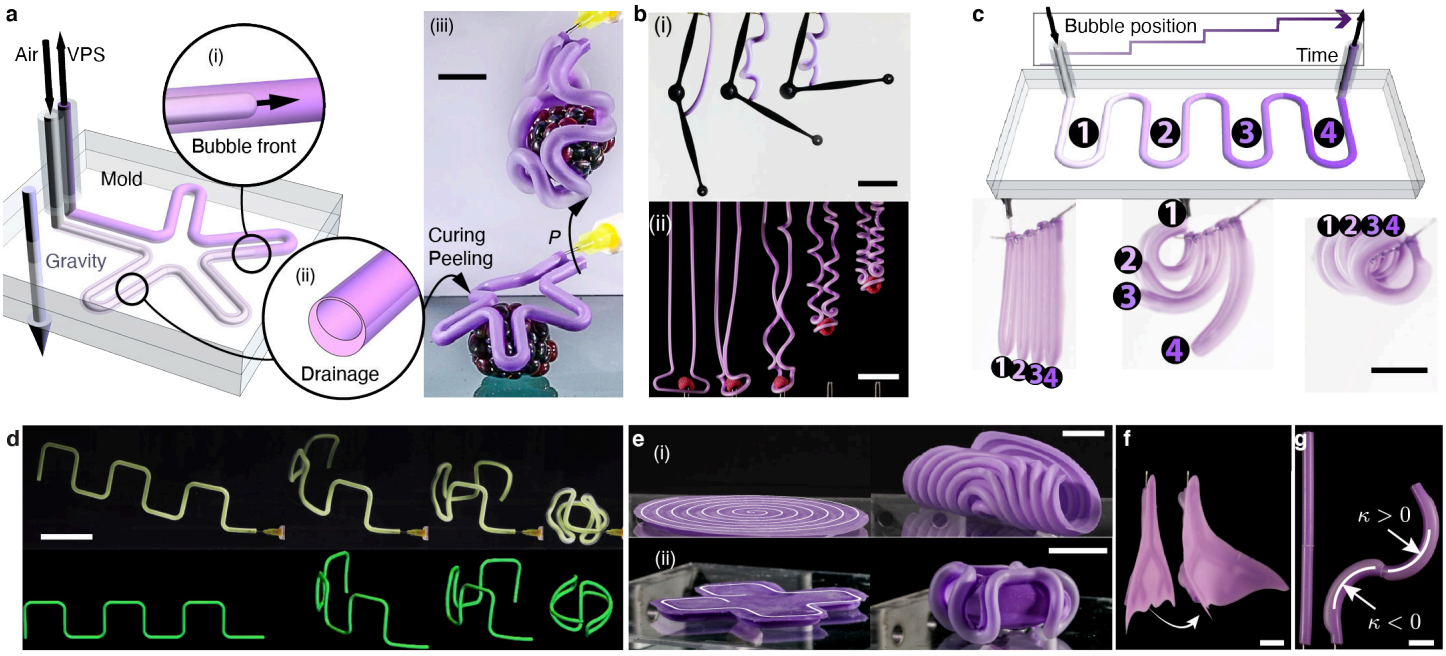

Figure 1: **From flow to programmed actuation.** (**a**) Schematic of the *bubble Casting* fabrication methodology. A bubble is injected (i) in a mold previously flooded with polymer melt. The residue of polymer drains (ii) and cure to provide a anisotropic actuator that can be readily used when de-molded, e.g. as a gripper (iii) (scale-bar: 1 cm). (**b**) Contractile coiling of long actuators yielding: (i) muscle-like contraction and (ii) linear translation (scale-bars: 5cm). (**c**) The bubble casting dynamics is used to program the deformation of an actuator, i.e. displaying sequential flexion of the four labeled digits following inflation via a simple pressure ramp (scale-bar: 1 cm). Morphing dynamics of (**d**) a curvilinear actuator (experiments and numerical simulation) submerged in a density matched fluid (scale-bar: 2 cm). (**e**) (i) Spiral shaped actuator and (ii) cross-like actuator, both attached to a thin membrane (scale-bars: 2 cm). (**f**) "Fish tail" motion is obtained using bubble-casting in a branched network (scale-bar: 1 cm). (**g**) Actuator displaying curvature of equal magnitude but opposite signs obtained by rotating the mold at the gelation point of the polymer (scale-bar: 1 cm) (see Movie S4).

achieve versatile and programmable actuators. We first fully rationalize the fluid mechanics at play during the bubble injection and the drainage to predict the shape of the actuators' cross-section. We then turn to the elastic problem to elucidate how the bending motion upon inflation is determined by the shape previously sculpted. We leverage these quantitative results to design actuators programmed for specific tasks through *bubble casting* such as soft robotic muscles with tunable strength capable of lifting objects (Fig. 1b and Movie S2) and soft fingers with sequential actuation from a single pressure source (Fig. 1c and Movie S3). Additionally, controlled folding in three dimension is demonstrated using curvilinear actuators, either free (Fig. 1d) or attached to thin membranes (Fig. 1e-f). Finally, we show that bending in different directions can be achieved by rotating portions of the mold relative to each other around the gelation point of the polymer [29] (Fig. 1g and Movie S4).

The shape of the cross section of our actuators is imparted by a two-fold process (Fig. 1a). First, the injection of the air bubble in the uncured melt results in the deposition of a thin polymer annulus in the mold, then the concomitant gravity-driven drainage and curing of the elastomer sculpt the final shape. We first consider the shape of the cross-section prior to drainage, right after the bubble injection. The flow at the front of the advancing bubble (Fig. 2a) leaves an annulus of constant thickness h_i. Fig. 2b shows this thickness in dimensionless form h_i/R as a function of the dimensionless bubble speed or capillary number $\mathrm{Ca} = \mu U/\gamma$, with R the radius, μ the melt viscosity, U the bubble velocity, and γ the melt surface tension. The data for different polymers and tube radii fall on a master curve showing that the thickness first increases with the velocity until it eventually saturates for $\mathrm{Ca} \gtrsim 3$.

This master curve can be understood from balanc-

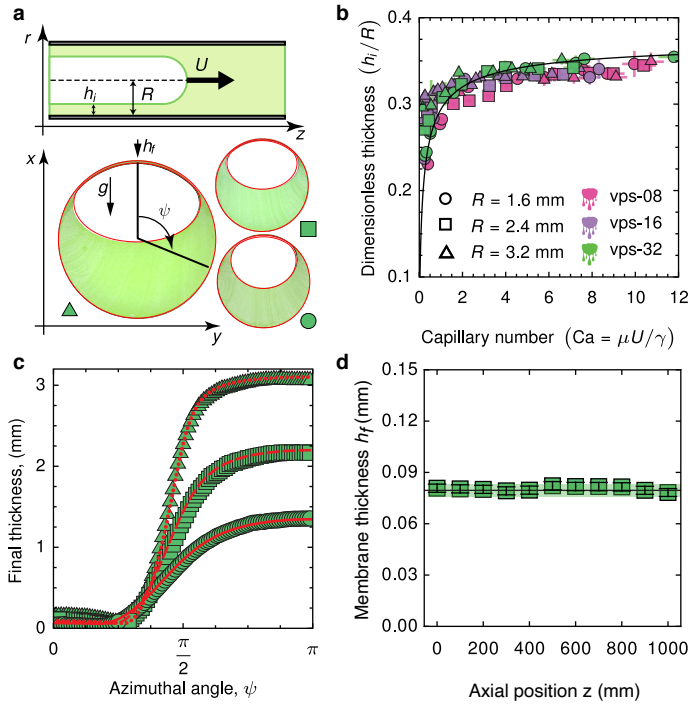

Figure 2: (**a**) Schematic of the Bretherton problem and photographs of the subsequent final cross-section post drainage. VPS-32 actuators with working time $\tau_w = 300$s and radius $R = \{3.2, 2.4, 1.6\}$ mm, the red lines show our prediction (See SI S2). (**b**) Dimensionless Bretherton film thickness h_i/R plotted against the Capillary Number $\mathrm{Ca} = \mu_0 U/\gamma$. The solid line is theory (Eq. 1) with $\beta = 2.65$. (**c**) Film thickness of the samples in (**a**) plotted against the central angle ψ. The red lines are theoretical predictions (identical to **a**). (**d**) Average thickness of the membrane h_f over a meter long sample (R=2.4mm). The black line shows our prediction while the green band accounts for parameters uncertainty.

ing viscous and capillary forces in the advancing meniscus [30–32] (see SI S1) yielding:

$$\frac{h_i}{R} = \frac{1.34\mathrm{Ca}^{2/3}}{1 + 1.34\beta\mathrm{Ca}^{2/3}}. \qquad (1)$$

We plot Eq. 1 with $\beta = 2.65$ along our data in Fig. 2b and find a good agreement. The melt annulus thickness, and hence the void fraction of the actuator, can thus be tuned by controlling the bubble velocity. In particular, using $\mathrm{Ca} \gtrsim 3$ robustly results in $h_i \sim 0.3R$.

The drainage of the annular polymer film left after bubble injection eventually sculpts the cross-section of our actuators shown in Fig. 2a. As evident from Fig. 2c which shows the thickness along the central angle ψ defined in Fig. 2a, the final shape consists of an upper thin film ($\psi \lesssim \pi/4$) of quasi uniform thickness connected to a thicker region at the bottom.

We first consider the upper thin film drainage driven by gravity g and resisted by viscosity [33]. To predict the final thickness, we must account for the time varying viscosity of our melt $\mu(t)$ as it solidifies. Our rheological measurements (see SI S3.1) are well described by the function $\mu(t) = \mu_0(1 - t/\tau_c)^{-n}$ which diverges at $t = \tau_c$ the curing time. The values of the initial viscosity μ_0, the curing time τ_c and the exponent and $n \simeq 2$ are fitted from the data, while the density of the melt ρ is assumed constant (see Table S1). Accounting that the drainage starts at a time $t = \tau_w$ after the reagents are mixed and finish at $t = \tau_c$, we include the viscosity variations in our drainage model [34] (see SI S2.4) and predict the final thickness to be:

$$h(\tau_c) = \sqrt{\frac{3\mu_0 R(n+1)\tau_c^{n+1}}{2\rho g \tau_c(\tau_c - \tau_w)^{n+1}}}. \qquad (2)$$

Note that the final film thickness does not depend on the initial film thickness.

We then consider the lower thick part of the cross-sections in Fig. 2a. The shape of this bath results from the competition between gravity and capillarity, yielding the Young-Laplace equation that we solve numerically under the proper constraints (see SI S2.2). Finally, we match the upper film and lower bath to obtain the final thickness profile along the whole cross-section (see SI S2.5). Our model produces the curves overlaid on images of the cross-section in Fig. 2a and the theoretical thickness profile plotted along typical experimental data on Fig. 2c. The agreement is favorable, demonstrating that we have accurately modeled the flow physics of our method.

Note that *bubble casting* does not require external control so that fluid mechanics alone dictates the actuator shape, thereby making this methodology extremely robust. While the membrane thickness is the order 100 μm, we obtain meter long samples that are virtually uniform (see Fig. 2d). Importantly, we can continuously and predictably tune the membrane average thickness h_f through the waiting time τ_w since $h_f \sim (\tau_c/(\tau_c - \tau_w))^{\frac{n+1}{2}}$ (see Eq. 2). In turn, the membrane thickness will play a key role in the actuator response to inflation as detailed next.

Upon inflation, the upper membrane of our *bubble casted* actuators stretches significantly more than its lower part, thereby creating a torque that bends the

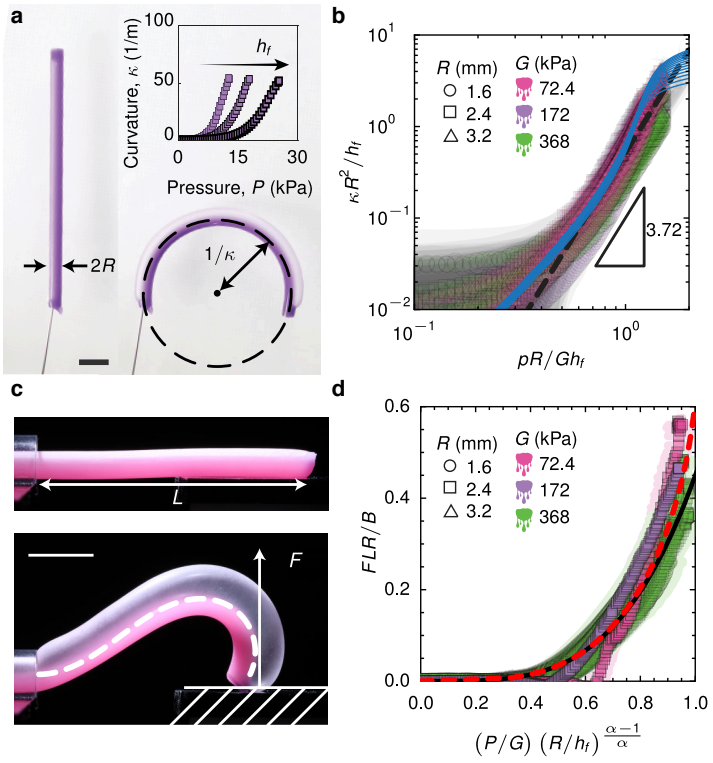

Figure 3: (**a**) Pictures of a VPS-16 actuator at rest and inflated at constant pressure: the actuator bends with a uniform curvature κ (Scale-bar: 1 cm). Inset: actuator curvature κ as a function of applied pressure P as the thickness is independently varied: $h_f = \{130, 165, 273\}$ μm. (**b**) Rescaled dimensionless curvature $\kappa R^2/h_f$ plotted against the rescaled pressure PR/Gh_f. The solid blue lines correspond to the energy minimization theory Eq. S28 for the relevant range of parameters (see SI S4.3). The dashed line is the scaling law Eq. 3 with a prefactor of 0.52. The gray shaded region represents the propagated experimental uncertainty. (**c**) Pictures of VPS-08 at rest and inflated in a blocking force configuration (Scale-bar: 1 cm). The force F is measured and reported in (**d**). The black (resp. red-dotted) line shows the linear (nonlinear) beam theory prediction (see SI S5.2).

actuator (Fig. 3a). In absence of other forces, the actuator bends on its whole length and adopts a uniform curvature κ as shown in Fig. 3a. The pressure required to bend the actuator is independent of its length but increases with the elastic shear modulus G, outer radius R and most importantly with the membrane thickness h_f (Fig. 3a and Fig .S6c). Predicting the deformation of an actuator is amenable to 3D finite element simulations (see SI S4.2), which further confirm that the lower region of the actuator is virtually undeformed while the upper thin membrane is under quasi isotropic stretch (Fig. S5a). This observation allows us to derive a simplified theoretical treatment of the problem (see SI S4.3), which combined with dimensional analysis suggests that the rescaled curvature $\kappa R^2/h_f$ only depends on the rescaled pressure PR/Gh_f (see SI S4.4).

In Fig. 3b we show that following this rescaling provides a reasonable collapse of our data. The resulting master curve exhibits a power law in the useful range of curvature ($\kappa/R > 10^{-2}$) that we fit and recast to obtain the relationship:

$$\kappa R \sim \left(\frac{P}{G} \left(\frac{R}{h_f} \right)^{\frac{\alpha-1}{\alpha}} \right)^{\alpha}, \qquad (3)$$

with $\alpha = 3.72 \pm 0.07$.

Further, we model our actuators as elastic rods [35] with effective natural curvature κ varying according to Eq. 3 when pressure is applied. We solve this centerline based model to predict the deformation of the actuators in the presence of external loads (see SI S5.2), e.g. when blocked from bending by a wall (Fig. 3c). We find that the overall shape of the actuator and the blocking force $F(P)$ exerted in this setup are well captured by our reduced order model when varying independently the actuator bending stiffness B, shear modulus G, length L, radius R, and thickness h_f (see Fig. 3d), thereby validating the approximations introduced in our model. Importantly, this model allows us to program the mechanical response of our actuators via the shape of their cross-section as detailed next. In our framework, solving the inverse design problem, i.e. finding the actuator that will morph to a target curvature, merely requires to invert the scaling law in Eq. 3.

Now that we have modeled how our actuators bend and behave as elastic rods, we demonstrate how to leverage this knowledge to design soft robotic muscles inspired by cucumber tendrils [36]. These muscles can be used over a wide range of size and strength (Fig. 4a,b) and can be integrated to programmable soft machines (Fig. 4c).

When subject to gravity, the curvature imparted by the actuation pressure competes with the actuator weight and generates a curling motion (see Fig. 4a). These shapes are analogous to the static configurations obtained with naturally curved elastic rods [37] and are well captured by our centerline-based theory. In Fig. 4d we show that our robotic muscles can contract up to $1 - \ell/L \approx 80\%$ of their initial length before entering in self-contact, exceeding the stroke of typical pneumatic

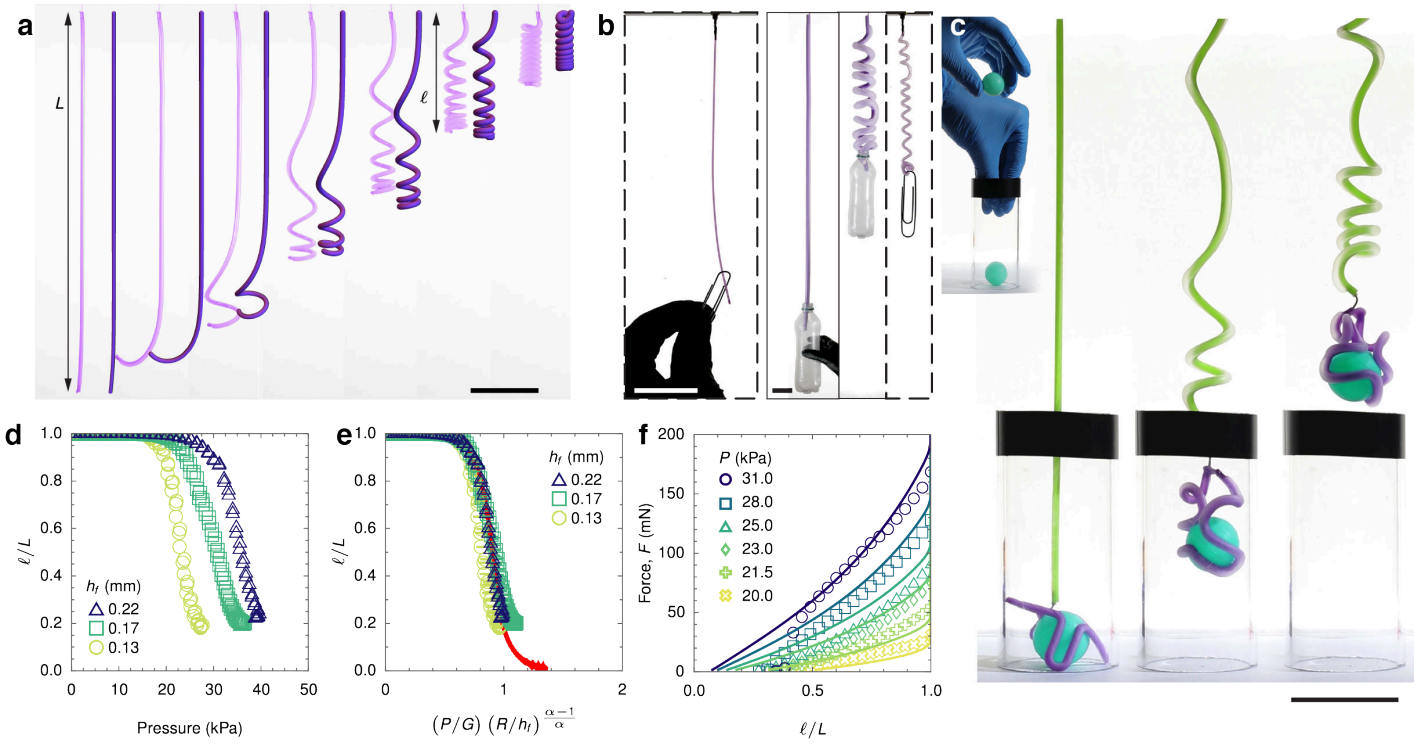

Figure 4: (**a**) Contractile coiling of an actuator formed in a rectilinear mold. Experiments and model are shown side-by-side (see SI S5; scale-bar: 5 cm). (**b**) Pictures of two VPS-16 robotic muscles of $R = 6.4$ and 0.5 mm lifting an empty bottle and a paperclip (scale-bars: 4 cm). (**c**) Pictures of a soft machine gripping and lifting a ball from a narrow cylinder (scale-bar: 5 cm). (**d**) Contraction ℓ/L (see **a**) as a function of the applied pressure for actuators with different apex thicknesses $h_f = \{0.14, 0.17, 0.22\}$ mm. (**e**) Same data shown as a function of the dimensionless pressure. The red curve is the result of Kirchhoff rod simulations (see SI S5). VPS-16, shear modulus $G = 172$ kPa, outer radius $R = 1.6$ mm and length $L = 320$ mm. (**f**) Force-elongation curves of a typical actuator at different pressure. The solid curves are the result of the equivalent Kirchhoff rod simulations (see SI S5).

muscles [38]. As evident from the figure, the transition between the extended and contracted configurations is sharp and occurs for values of pressure varying with h_f. In Fig. 4e we show that the variation of the free-hang length with pressure collapses when using Eq. 3 combined to our rod model, further confirming the validity of our rod theory in the limit of very large deformations. As such, we can predict and tune the pulling force exerted by these muscles. For instance, in Fig. 4f we show that the effective stiffness of our muscles can be smoothly varied via the applied pressure. This level of control allows us to program soft machines capable of achieving complex tasks, such as fetching a ball sitting at the bottom of a narrow cylinder (Fig. 4c and Movie S5). This contraption comprises two interconnected building blocks reverse engineered using Eq. 3 to sequentially grip and then pull a ball following the monotonic increase of a *single* pressure source.

Programming can also be achieved using fluid mechanics alone, i.e. modulating the membrane thickness h_f via eq. 2. For instance, using a programmed sequence of injection of the bubble where τ_w increases by step across a sample, we readily cast an actuator with four different values of h_f, each confined to a "finger" of the actuator (see Fig. 1c). As a result, an increase of the pressure in this monolithic actuator leads to the sequential bending of each finger shown in Fig. 1c and Movie S3. Likewise, we can solve the inverse problem where a simple target shape can be obtained by carefully choosing τ_w across the actuator (see Movie S6).

In closing, we note that *Bubble casting* is a bonding-free fabrication method that relies on the fluid flow instead of an internal template to build a void. This reliance on continuum mechanics as opposed to machined

parts allows for defect free fabrication of soft pneumatic actuators over a wide range of sizes (see Fig. 1 and 4) and previously impossible aspect ratios. In particular, the thin membranes we achieve optimize the eccentric void topology and outperform most inflatable actuators in terms of bending coefficients (defined as the ratio between the curvature and the applied pressure at a bending deformation of 90^o [25]). Further, the unconstrained internal surface makes the construction of curved and network actuators that achieve 3D folding shapes (Fig. 1d-f and Movie S4) as simple as building straight actuators. These new capabilities will resonate in the soft matter community, and, in particular could lead to new generation robotic materials suited to move and interact with their environment while maintaining tractable complexity. More generally, our methodology falls under the category of approaches leveraging out-of-equilibrium fluidic processes to revolutionize our ability to build structures, e.g. relying on instabilities [39, 40], shear-flow [41], Marangoni effects [42] and centrifugal forces [43].

Methods

To make our actuators we used vinyl polysiloxane (VPS), Zhermack elite double 8, 16, and 32 silicone elastomers ($G = 72.4, 172, 368$ kPa respectively). The catalyst and prepolymer base were mixed in a 1:1 weight ratio in a centrifugal mixer for 10 s at 2,000 rpm (clockwise) and 10 s at 2,200 rpm (counterclockwise) at room temperature. The resulting polymer melt (rheology described in SI S3.1) was injected into a mold where we then followed our *bubble casting* method, as described in the text. For the molds we used cellulose tubes ($R = 1.6, 2.4, 3.2, 6.4$ mm), glass tubes ($R = 0.5$ mm), and cast acrylic sheets carved with a cnc milling tool on one side.

Schematics for our experiments are shown in Fig. S4. The bubble velocity, curvature data, and free-hang length was recorded using a camera and image processing in Python. Since the final drainage loses memory of the initial condition (as described in the text), we often injected the bubble early and reset τ_w by flipping the mold. This allowed us to maintain constant drainage timing along the length of long actuators. To attach the thin membranes shown in Fig. 1e,f, the two sides of the carved molds (see Fig. 1a) were separated. Some more polymer was then spin-coated on top of the actuator still encased in the mold. We realized the experiment show in Fig. 1g by joining two tubes using a 3D printed tube connector. When the polymer is at the gelation point one tube is carefully rotated relative to the other (see Fig. S8). The cross-section profiles were obtained post curing using an optical microscope and ImageJ. Pressure data was measured using a differential pressure sensor (MPX5100dp) connected to a data acquisition board (Arduino). To measure the pulling force, we attached the actuator to an Instron and performed tensile tests. The blocking force was measured by placing the free end of the actuator on a plate fitted to a load cell. The curvature of our actuators was measured without external forces (e.g. gravity) by floating the elastomer on a water bath. Actuator mechanics were measured quasi-statically by slowly injecting air in 1 s pulses and waiting 4 s between pulses. All actuators were pierced with syringe needles and inflated by a syringe mounted on a syringe pump (Harvard Apparatus).

Acknowledgments

E.J.-P. was partially supported by NSF through the Princeton University Materials Research Science and Engineering Center (Grant DMR-1420541) and TJJ was partially supported by NSF CAREER award (CBET 2042930)

Author Contributions

T.J.J., J.M., and P.-T.B. conceived the project. T.J.J., E.J.-P., and P.-T.B. conducted the experiments and analyzed the data. T.J.J. performed the Kirchhoff rod simulations. E.J.-P. performed the finite element simulations. All authors wrote the manuscript.

Data availability

The authors declare that the main data supporting the findings of this study are available within the article and its Supplementary Information files. Extra data are available from the corresponding author upon request.

References

[1] George M Whitesides. Soft robotics. *Angewandte Chemie International Edition*, 57(16):4258–4273, 2018.

[2] Panagiotis Polygerinos, Zheng Wang, Kevin C Galloway, Robert J Wood, and Conor J Walsh. Soft

robotic glove for combined assistance and at-home rehabilitation. *Robotics and Autonomous Systems*, 73:135–143, 2015.

[3] Robert F Shepherd, Filip Ilievski, Wonjae Choi, Stephen A Morin, Adam A Stokes, Aaron D Mazzeo, Xin Chen, Michael Wang, and George M Whitesides. Multigait soft robot. *Proceedings of the national academy of sciences*, 108(51):20400–20403, 2011.

[4] Ramses V Martinez, Jamie L Branch, Carina R Fish, Lihua Jin, Robert F Shepherd, Rui MD Nunes, Zhigang Suo, and George M Whitesides. Robotic tentacles with three-dimensional mobility based on flexible elastomers. *Advanced materials*, 25(2):205–212, 2013.

[5] Ellen T Roche, Robert Wohlfarth, Johannes TB Overvelde, Nikolay V Vasilyev, Frank A Pigula, David J Mooney, Katia Bertoldi, and Conor J Walsh. A bioinspired soft actuated material. *Advanced Materials*, 26(8):1200–1206, 2014.

[6] Bobak Mosadegh, Panagiotis Polygerinos, Christoph Keplinger, Sophia Wennstedt, Robert F Shepherd, Unmukt Gupta, Jongmin Shim, Katia Bertoldi, Conor J Walsh, and George M Whitesides. Pneumatic networks for soft robotics that actuate rapidly. *Advanced functional materials*, 24(15):2163–2170, 2014.

[7] Hong Kai Yap, Hui Yong Ng, and Chen-Hua Yeow. High-force soft printable pneumatics for soft robotic applications. *Soft Robotics*, 3(3):144–158, 2016.

[8] Michael Wehner, Ryan L Truby, Daniel J Fitzgerald, Bobak Mosadegh, George M Whitesides, Jennifer A Lewis, and Robert J Wood. An integrated design and fabrication strategy for entirely soft, autonomous robots. *Nature*, 536(7617):451–455, 2016.

[9] Huichan Zhao, Yan Li, Ahmed Elsamadisi, and Robert Shepherd. Scalable manufacturing of high force wearable soft actuators. *Extreme Mechanics Letters*, 3:89–104, 2015.

[10] Jungwook Paek, Inho Cho, and Jaeyoun Kim. Microrobotic tentacles with spiral bending capability based on shape-engineered elastomeric microtubes. *Scientific reports*, 5:10768, 2015.

[11] Lishuai Jin, Antonio Elia Forte, Bolei Deng, Ahmad Rafsanjani, and Katia Bertoldi. Kirigami-inspired inflatables with programmable shapes. *Advanced Materials*, 32(33):2001863, 2020.

[12] Filip Ilievski, Aaron D Mazzeo, Robert F Shepherd, Xin Chen, and George M Whitesides. Soft robotics for chemists. *Angewandte Chemie International Edition*, 50(8):1890–1895, 2011.

[13] Andrew D Marchese, Cagdas D Onal, and Daniela Rus. Autonomous soft robotic fish capable of escape maneuvers using fluidic elastomer actuators. *Soft robotics*, 1(1):75–87, 2014.

[14] Dian Yang, Mohit S Verma, Ju-Hee So, Bobak Mosadegh, Christoph Keplinger, Benjamin Lee, Fatemeh Khashai, Elton Lossner, Zhigang Suo, and George M Whitesides. Buckling pneumatic linear actuators inspired by muscle. *Advanced Materials Technologies*, 1(3):1600055, 2016.

[15] Johannes TB Overvelde, Tamara Kloek, Jonas JA D'haen, and Katia Bertoldi. Amplifying the response of soft actuators by harnessing snap-through instabilities. *Proceedings of the National Academy of Sciences*, 112(35):10863–10868, 2015.

[16] Elliot W Hawkes, Laura H Blumenschein, Joseph D Greer, and Allison M Okamura. A soft robot that navigates its environment through growth. *Science Robotics*, 2(8), 2017.

[17] Carmel Majidi. Soft robotics: a perspective—current trends and prospects for the future. *Soft Robotics*, 1(1):5–11, 2014.

[18] A Sydney Gladman, Elisabetta A Matsumoto, Ralph G Nuzzo, Lakshminarayanan Mahadevan, and Jennifer A Lewis. Biomimetic 4d printing. *Nature materials*, 15(4):413–418, 2016.

[19] Mehmet Kanik, Sirma Orguc, Georgios Varnavides, Jinwoo Kim, Thomas Benavides, Dani Gonzalez, Timothy Akintilo, C Cem Tasan, Anantha P Chandrakasan, Yoel Fink, et al. Strain-programmable fiber-based artificial muscle. *Science*, 365(6449):145–150, 2019.

[20] J William Boley, Wim M van Rees, Charles Lissandrello, Mark N Horenstein, Ryan L Truby, Arda Kotikian, Jennifer A Lewis, and L Mahadevan. Shape-shifting structured lattices via multimaterial 4d printing. *Proceedings of the National Academy of Sciences*, 116(42):20856–20862, 2019.

[21] Ruslan Guseinov, Connor McMahan, Jesús Pérez, Chiara Daraio, and Bernd Bickel. Programming temporal morphing of self-actuated shells. *Nature communications*, 11(1):1–7, 2020.

[22] Yoonho Kim, Hyunwoo Yuk, Ruike Zhao, Shawn A Chester, and Xuanhe Zhao. Printing ferromagnetic domains for untethered fast-transforming soft materials. *Nature*, 558(7709):274–279, 2018.

[23] Wenqi Hu, Guo Zhan Lum, Massimo Mastrangeli, and Metin Sitti. Small-scale soft-bodied robot with multimodal locomotion. *Nature*, 554(7690):81–85, 2018.

[24] E Acome, SK Mitchell, TG Morrissey, MB Emmett, C Benjamin, M King, M Radakovitz, and C Keplinger. Hydraulically amplified self-healing electrostatic actuators with muscle-like performance. *Science*, 359(6371):61–65, 2018.

[25] Benjamin Gorissen, Dominiek Reynaerts, Satoshi Konishi, Kazuhiro Yoshida, Joon-Wan Kim, and Michael De Volder. Elastic inflatable actuators for soft robotic applications. *Advanced Materials*, 29(43):1604977, 2017.

[26] Panagiotis Polygerinos, Nikolaus Correll, Stephen A Morin, Bobak Mosadegh, Cagdas D Onal, Kirstin Petersen, Matteo Cianchetti, Michael T Tolley, and Robert F Shepherd. Soft robotics: Review of fluid-driven intrinsically soft devices; manufacturing, sensing, control, and applications in human-robot interaction. *Advanced Engineering Materials*, 19(12):1700016, 2017.

[27] Emmanuel Siéfert, Etienne Reyssat, José Bico, and Benoît Roman. Bio-inspired pneumatic shape-morphing elastomers. *Nature materials*, 18(1):24, 2019.

[28] Nikolaos Vasios, Andrew J Gross, Scott Soifer, Johannes TB Overvelde, and Katia Bertoldi. Harnessing viscous flow to simplify the actuation of fluidic soft robots. *Soft Robotics*, 7(1):1–9, 2020.

[29] Etienne Jambon-Puillet, Matthieu Royer Piéchaud, and P-T Brun. Elastic amplification of the rayleigh–taylor instability in solidifying melts. *Proceedings of the National Academy of Sciences*, 118(10), 2021.

[30] Francis Patton Bretherton. The motion of long bubbles in tubes. *Journal of Fluid Mechanics*, 10(2):166–188, 1961.

[31] Pascale Aussillous and David Quéré. Quick deposition of a fluid on the wall of a tube. *Physics of fluids*, 12(10):2367–2371, 2000.

[32] Evert Klaseboer, Raghvendra Gupta, and Rogerio Manica. An extended bretherton model for long taylor bubbles at moderate capillary numbers. *Physics of Fluids*, 26(3):032107, 2014.

[33] Daisuke Takagi and Herbert E Huppert. Flow and instability of thin films on a cylinder and sphere. *Journal of Fluid Mechanics*, 647:221–238, 2010.

[34] Anna Lee, P-T Brun, J Marthelot, G Balestra, F Gallaire, and Pedro M Reis. Fabrication of slender elastic shells by the coating of curved surfaces. *Nature communications*, 7(1):1–7, 2016.

[35] Basile Audoly and Yves Pomeau. *Elasticity and geometry: from hair curls to the non-linear response of shells*. Oxford university press, 2010.

[36] Sharon J Gerbode, Joshua R Puzey, Andrew G McCormick, and L Mahadevan. How the cucumber tendril coils and overwinds. *Science*, 337(6098):1087–1091, 2012.

[37] JT Miller, Arnaud Lazarus, Basile Audoly, and Pedro M Reis. Shapes of a suspended curly hair. *Physical review letters*, 112(6):068103, 2014.

[38] Hee Doo Yang, Brandyn T Greczek, and Alan T Asbeck. Modeling and analysis of a high-displacement pneumatic artificial muscle with integrated sensing. *Frontiers in Robotics and AI*, 5:136, 2019.

[39] Joshua J Kaufman, Guangming Tao, Soroush Shabahang, Esmaeil-Hooman Banaei, Daosheng S Deng, Xiangdong Liang, Steven G Johnson, Yoel Fink, and Ayman F Abouraddy. Structured spheres generated by an in-fibre fluid instability. *Nature*, 487(7408):463–467, 2012.

[40] J Marthelot, EF Strong, Pedro M Reis, and P-T Brun. Designing soft materials with interfacial instabilities in liquid films. *Nature communications*, 9(1):1–7, 2018.

[41] Chuangqi Zhao, Pengchao Zhang, Jiajia Zhou, Shuanhu Qi, Yoshihiro Yamauchi, Ruirui Shi, Ruochen Fang, Yasuhiro Ishida, Shutao Wang, Antoni P Tomsia, et al. Layered nanocomposites by shear-flow-induced alignment of nanosheets. *Nature*, 580(7802):210–215, 2020.

[42] Bryan A Nerger, P-T Brun, and Celeste M Nelson. Marangoni flows drive the alignment of fibrillar cell-laden hydrogels. *Science advances*, 6(24):eaaz7748, 2020.

[43] Olgierd Cybulski, Miroslaw Dygas, Barbara Mikulak-Klucznik, Marta Siek, Tomasz Klucznik, Seong Yeol Choi, Robert J Mitchell, Yaroslav I Sobolev, and Bartosz A Grzybowski. Concentric liquid reactors for chemical synthesis and separation. *Nature*, 586(7827):57–63, 2020.